was greater than 99%, and the yield was 42.4±3.2% (EOB). The specific activity calculated by the analytical HPLC system was more than 111 GBq/μmol.

2.3. PET imaging

All subjects fasted more than 4 h prior to FES PET examination to eliminate the excretion of FES from the hepatobiliary system and the gastrointestinal tract, which would otherwise interfere with image interpretation in the pelvic space. Three milliliters of blood was obtained just before FES injection to measure the endogenous estrogen level [estradiol (E2)]. FES PET data acquisition started 60 min after the injection of 185 MBq of FES. Emission scans were performed for 3 min in the pelvic portion (two bed positions) and for 2 min in the remaining positions (five bed positions) to cover the area from the head to the inguinal region. Postinjection transmission scans for 2 min at the pelvis and for 1 min in other parts were performed after the emission scans for attenuation correction. The acquired data were reconstructed using an iterative reconstruction method with 14 subsets and two iterations. The reconstructed image was converted to standardized uptake value (SUV) image according to the subject's body weight and net injected dose for the data analysis.

2.4. Magnetic resonance imaging

All subjects underwent MRI examination on the same day FES PET was performed or 1 day before FES PET was carried out to obtain positional information regarding the endometrium and myometrium. T_1- and T_2-weighted images (WIs) in the transaxial plane and T_2-WI in the sagittal plane were acquired using a 1.5-T superconducting MRI system (Signa, GE Medical Systems). The imaging sequence of T_1-WI and T_2-WI was 533/8 and 4700/90 ms (TR/TE), respectively.

2.5. Data analysis

On the midsagittal image of FES PET, circular regions of interest (ROIs: 8 mm in diameter) were placed using guidance by T_2-WI of MRI in the sagittal plane. By comparing FES PET and MRI visually, the endometrium, which usually has high uptake of FES compared with the myometrium, was identified. The myometrium was defined as the faint FES uptake area surrounding the endometrium. Three ROIs were placed on the endometrium and nine were placed on the myometrium, as shown in Fig. 1. The averaged SUVs in the endometrium and myometrium were plotted against the number of days from the onset of menses and the endogenous estrogen level.

In this study, the menstrual cycle was classified into two groups because of the limited number of subjects: (1) the proliferative phase (6 to 14 days after the onset of menses) and (2) the secretory phase (15 to 28 days from the onset of menses). SUVs between these two phases were compared in the endometrium and myometrium. Nonparametric Mann–Whitney U test was used for statistical comparisons. Spearman nonparametric correlation analysis was performed to analyze the relationship between SUVs in both the endometrium and the myometrium and E2. In each statistical analysis, $P<.05$ was considered to represent statistical significance.

3. Results

Characteristics of the subjects and a summary of the results are shown in Table 1.

One subject had an irregular menstrual cycle and was excluded from the analysis regarding the relationship between FES uptake and menstrual cycle. Based on the menstrual cycle classification mentioned in the Data analysis section, six subjects were classified as being in the proliferative phase and seven were classified as being in

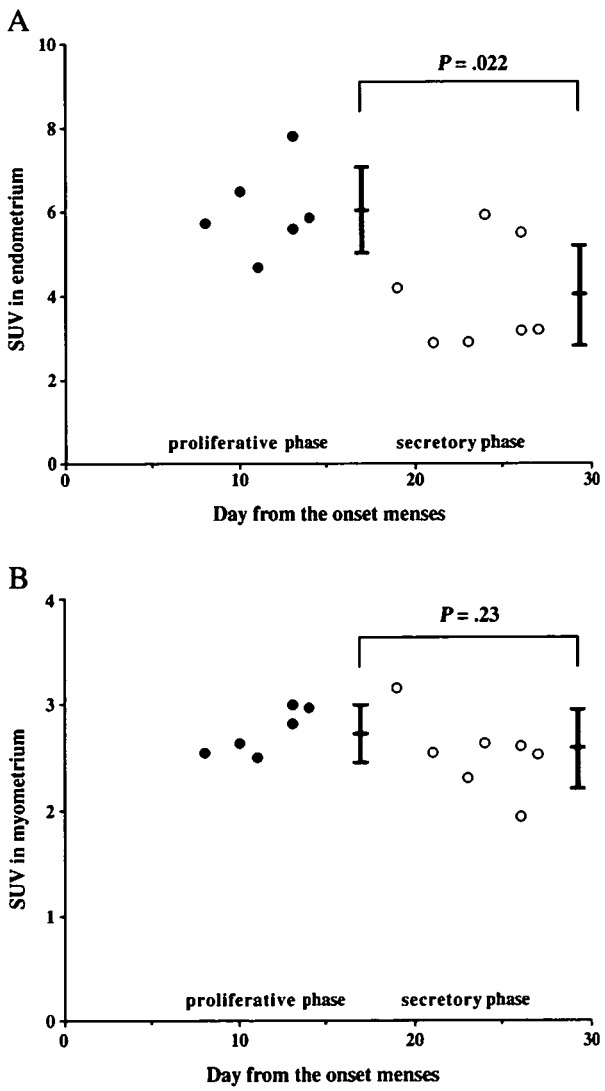

Fig. 2. Changes in FES uptake in the uterus during the menstrual cycle. Endometrial FES uptake (A) was significantly higher in the proliferative phase (filled circle) than in the secretory phase (open circle). By contrast, myometrial FES uptake (B) was similar when the two phases are compared.

the secretory phase. Two subjects were in the menstrual phase and were also excluded from this analysis. In the analysis of the relationship between FES uptake and E2 level, no subjects were excluded.

Fig. 2A shows the relationship between endometrial SUV and the menstrual cycle. SUV was significantly higher in the proliferative phase than in the secretory phase (6.03±1.05 vs. 3.97±1.29, P=.022).

The relationship between myometrial SUV and the menstrual cycle is illustrated in Fig. 2B. No significant difference in SUV was noted when the proliferative and secretory phases were compared (2.75±0.22 vs. 2.53±0.37, P=.23).

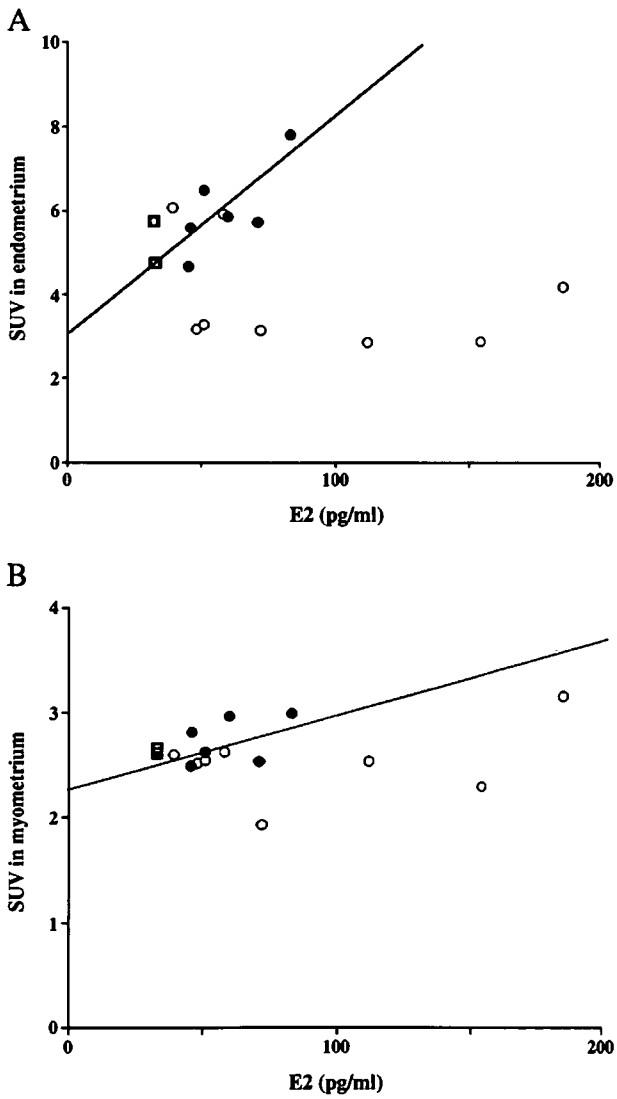

Fig. 3. Relationship between FES uptake and endogenous estrogen level. Linear regression analysis (solid line) was performed only in the proliferative phase (filled circle). No significant linear correlation was observed in the endometrium (A) (y=0.05x+2.95, r^2=.56, P=.09) or the myometrium (B) (y=0.006x+2.37, r^2=.20, P=.38). Open circles represent SUV in the proliferative phase, and open squares represent SUV in the menstrual phase.

Further, there was no relationship between FES uptake and E2 level in the endometrium (Fig. 3A) or myometrium (Fig. 3B) in the proliferative phase.

4. Discussion

Physiological FES uptake in the endometrium is affected by the menstrual cycle secondary to changes in endogenous estrogen level in healthy women. However, the present study demonstrated that endometrial SUV was not directly correlated with plasma E2 level or FES uptake in the myometrium. Yoo et al. [19] reported that FES preferentially binds the ERα subtype with 6.3-fold higher affinity than that for ERβ. Further, the uterus is one of the target organs of E2 and expresses both ERα and ERβ. ERα predominates in the uterus, breast, kidney, liver and heart, whereas tissues that have high ERβ levels include those of the prostate, testes, ovaries, gastrointestinal tract, lung, bladder and hematopoietic and central nervous systems. Many tissues contain both ERα and ERβ, such as breast, epididymis, thyroid, adrenal and bone tissues. Wang et al. [20] used immunohistochemistry to demonstrate that the myometrium and leiomyomas have ERα-dominant expression. These results suggested that uterine ER expression is a good target for study with FES PET. However, physiological FES uptake in the uterus of healthy women remains unclear and may vary with the menstrual cycle observed in FDG PET [21].

Several investigators have used immunohistochemistry to characterize the relationship between ER expression and menstrual cycle measured in the endometrium [8–17] and myometrium [9–16]. In these reports, endometrial ER concentration in the proliferative phase was higher than that in the secretory phase, which is consistent with results from the present study. Further, several studies have reported a significant difference between myometrial ER concentration in the proliferative and secretory phases. By contrast, the present study showed no significant difference in myometrial FES uptake when the proliferative and secretory phases were compared. This finding is supported by some papers [14–16]. Noe et al. [15] and Vienonen et al. [16] reported that in the myometrium, ERα was regulated in the layer adjacent to the endometrium in an endometrium-like pattern during the menstrual cycle, whereas expression pattern in the outer part of the myometrium was more stable. In the studies that showed a significant difference between myometrial ER concentration in the proliferative and secretory phases, only the myometrium immediately underlying the endometrium was analyzed as the representative of the whole uterine muscular wall [9–11]. In the present study, ROIs that were placed on the myometrium, which surrounded endometrial ROIs, evaluated the outer part of the myometrium because of the limited spatial resolution.

In this study, there was no significant relationship between FES uptake and E2 even in the proliferative phase. A previous study reported that a large concentration of endometrial ER in

the late proliferative phase correlates with the plasma E2 surge [22]. Further, Levy et al. [8] reported that a significant correlation was observed between ER concentration and E2 in the proliferative phase. In the present study, there was a trend toward a relationship between E2 and SUV in the endometrium in the proliferative phase ($P=.09$), but the difference did not reach the level of statistical significance. Repetition of the present study with a large population size may result in data consistent with those reported by Levy et al.

The relationship between ER concentration in the myometrium and endogenous estrogen level demonstrated no statistical significance. FES uptake in the myometrium was almost constant throughout the entire menstrual cycle and may be independent from the change of endogenous estrogen level in healthy volunteers.

Although FES represents the level of unoccupied ER and ER measured with immunohistochemistry represents total ER, our results and the previous reports showed the same behavior. Katzenellenbogen et al. [23] reported that the FES uptake in the uterus was suppressed by the coinjection of a high dose of E2 or the tamoxifen pretreatment in the rat. However, although total ER and occupied ER by endogenous estrogen in the endometrium will increase in the proliferative phase, the proportion of unoccupied ER measured with FES will not change. In the secretory phase, the opposite phenomenon will occur and the proportion of unoccupied ER will not change as well. Therefore, it is speculated that the behavior of total ER and unoccupied ER will be similar. In the myometrium, total and unoccupied ER in the proliferative phase did not change when the endogenous estrogen increased. The proportion of occupied ER against total ER may be small enough, although further examination will be required.

FES has been used for the evaluation of breast tumors [2–6] and may also have a clinical application in patients with uterine endometrium-related gynecological diseases [24,25]. Indeed, Okazawa et al. [25] reported that the combination of FDG PET and FES PET improved the diagnostic accuracy in various uterine endometrium-related gynecological diseases including uterine endometrial cancer, adenomyosis and endometrial hyperplasia. For the assessment of FES uptake, SUV or lesion-to-normal ratio will be feasible. The present study demonstrated that FES uptake in the endometrium varied with the menstrual cycle, whereas myometrial FES uptake was stable throughout the entire menstrual cycle. These data suggest that the myometrium may serve as a good internal control during FES studies of other organ systems and that the menstrual cycle should be taken account of when the endometrium was considered for an internal control.

5. Conclusion

The change of ER concentration relative to menstrual cycle as characterized by FES was consistent with those from previous reports that used an immunohistochemical technique. Further, these data suggest that FES PET is a feasible, noninvasive method for characterizing changes in ER concentration.

Acknowledgments

The authors thank Miyuki Tamaru, Mika Ito and other staff members of the Biological Imaging Research Center, University of Fukui, for technical and clinical support. This study was partly funded by the Research and Development Project Aimed at Economic Revitalization (Leading Project) from MEXT Japan and by the 21st Century COE Program (Medical Science) from the Japan Society for the Promotion of Science.

References

[1] Kiesewetter DO, Kilbourn MR, Landvatter SW, Heiman DF, Katzenellenbogen JA, Welch MJ. Preparation of four fluorine-18-labeled estrogen and their selective uptake in target tissue of immature rats. J Nucl Med 1984;25:1212–21.
[2] Mintun MA, Welch MJ, Siegel BA, Mathias CJ, Brodack JW, McGuire AH, et al. Breast cancer: PET imaging of estrogen receptors. Radiology 1988;169:45–8.
[3] McGuire AH, Dehdashti F, Siegel BA, Lyss AP, Brodack JW, Mathias CJ, et al. Positron tomographic assessment of 16α-[^{18}F]fluoro-17β-estradiol uptake in metastatic breast carcinoma. J Nucl Med 1991;32:1526–31.
[4] Dehdashti F, Mortimer JE, Siegel BA, Griffeth LK, Bonasera TJ, Fusselman MJ, et al. Positron tomographic assessment of estrogen receptors in breast cancer: comparison with FDG-PET and in vitro receptor assays. J Nucl Med 1995;36:1766–74.
[5] Dehdashti F, Flanagan FL, Mortimer JE, Katzenellenbogen JA, Welch MJ, Siegel MA. Positron emission tomographic assessment of "metabolic flare" to predict response of metastatic breast cancer to antiestrogen therapy. Eur J Nucl Med 1999;26:51–6.
[6] Mortimer JE, Dehdashti F, Siegel BA, Trinkaus K, Katzenellenbogen JA, Welch MJ. Metabolic flare: indicator of hormone responsiveness in advanced breast cancer. J Clin Oncol 2001;19:2797–803.
[7] Nilsson S, Makela S, Treuter E, Tujague M, Thomsen J, Andersson G, et al. Mechanisms of estrogen action. Physiol Rev 2001;81:1535–65.
[8] Levy C, Robel P, Gautray JP, De Brux J, Verma U, Descomps B, et al. Estradiol and progesterone receptors in human endometrium: normal and abnormal menstrual cycle and early pregnancy. Am J Obstet Gynecol 1980;136:646–51.
[9] Lessey BA, Killan AP, Metzger A, Haney AF, Greene GL, McCarty KS. Immunohistochemical analysis of human uterine estrogen and progesterone receptors throughout the menstrual cycle. J Clin Endocrinol Metab 1988;67:334–40.
[10] Kawaguchi K, Fujii S, Konishi I, Iwai T, Nanbu Y, Nonogaki H, et al. Immunohistochemical analysis of oestrogen receptors, progesterone receptors and Ki-67 in leiomyoma and myometrium during menstrual cycle and pregnancy. Virchows Arch A Pathol Anat 1991;419:309–15.
[11] Snijders MPML, de George AFPM, Cetets-Te Baerts MJC, Rousch MJM, Koudstaal J, Bosman FT. Immunocytochemical analysis of oestrogen receptors and progesterone receptors in human uterus throughout the menstrual cycle and after the menopause. J Reprod Fertil 1992;94:363–71.
[12] Englund K, Blanck A, Gustavsson I, Lundkvist U, Sjöblom P, Norgren A, et al. Sex steroid receptors in human myometrium and fibrosis: changes during the menstrual cycle and gonadotropin-

releasing hormone treatment. J Clin Endocrinol Metab 1998;83: 4092–6.

[13] Mertens HJMM, Heineman MJ, Theunissen PHMH, de Jong FH, Evers JLH. Androgen, estrogen and progesterone receptor expression in the human uterus during menstrual cycle. Eur J Obstet Gynecol Reprod Biol 2001;98:58–65.

[14] Nisolle M, Gillerot S, Casanas-Roux F, Squifflet J, Berliere M, Donnez J. Immunohistochemical study of the proliferation index, oestrogen receptors and progesterone receptors A and B in leiomyoma and normal myometrium during menstrual cycle and under gonadotropin-releasing hormone agonist therapy. Hum Reprod 1999;14:2844–50.

[15] Noe M, Kunz G, Herbertz M, Mall G, Leyendecker G. The cyclic pattern of the immunocytochemical expression of oestrogen and progesterone receptors in human myometrial and endometrial layers: characterization of the endometrial–subendometrial unit. Hum Reprod 1999;14:190–7.

[16] Vienonen A, Miettinen S, Bläuer M, Martikainen PM, Tomás E, Heinonen PK, et al. Expression of nuclear receptors and cofactors in human endometrium and myometrium. J Soc Gynecol Investig 2004;11:104–12.

[17] Shiozawa T, Shih H, Miyamoto T, Feng Y-Z, Uchikawa J, Itoh K, et al. Cyclic changes in the expression of steroid receptor coactivators and corepressors in the normal human endometrium. J Clin Endocrinol Metab 2003;88:871–8.

[18] Mori T, Kasamatsu S, Mosdzianowski C, Welch MJ, Yonelura Y, Fujibayashi Y. Automatic synthesis of 16α-[^{18}F]fluoro-17β-estradiol using a cassette-type [^{18}F] fluorodeoxyglucose synthesizer. Nucl Med Biol 2006;33:281–6.

[19] Yoo J, Dence CS, Sharp TL, Katzenellenbogen JA, Welch MJ. Synthesis of an estrogen receptor β-selective radioligand: 5-[^{18}F]fluoro-(2*R**,3*S**)-2,3-bis (4-hydroxyphehyl)pentanenitrile and comparison of in vivo distribution with 16α-[^{18}F]fluoro-17β-estradiol. J Med Chem 2005;48:6366–78.

[20] Wang H, Wu X, Englund K, Masironi B, Eriksson H, Sahlin L. Different expression of estrogen receptors alpha and beta in human myometrium and leiomyoma during the proliferative phase of the menstrual cycle and after GnRHa treatment. Gynecol Endocrinol 2001;15:443–52.

[21] Nishizawa S, Inubushi M, Okada H. Physiological ^{18}F-FDG uptake in the ovaries and uterus of healthy female volunteers. Eur J Nucl Med Mol Imaging 2005;32:549–56.

[22] Robertson DM, Mester J, Beilby J, Steele SJ, Kellie AF. The measurement of high-affinity oestradiol receptors inhuman uterine endometrium and myometrium. Acta Endocrinol 1971;68:534–42.

[23] Katzenellenbogen JA, Mathias CJ, Vanbrocklin HF, Brodack JW, Welch MJ. Titration of the in vivo uptake of 16α-[^{18}F]fluoroestradiol by target tissues in the rat: comparison by tamoxifen, and implications for quantitating estrogen receptors in vivo and the use of animal models in receptor-binding radiopharmaceutical development. Nucl Med Biol 1993;20:735–45.

[24] Yoshida Y, Kurokawa T, Yagihara R, Kotsuji F. The usefulness of FES-PET for the prediction of the therapeutic effect of hormonal therapy in a patient with endometrial cancer — a case report (abstract). J Obstet Gynaecol Res 2006;58:406.

[25] Okazawa H, Yoshida Y, Mori T, Tsuchida T, Kurokawa T, Kobayashi M, et al. Evaluation of uterine endometrium related gynecological diseases using F-18 fluoroestradiol and PET (Abstract). J Nucl Med 2006;47:318.

資料(7)

資料 7

Available online at www.sciencedirect.com

ScienceDirect

ELSEVIER

Nuclear Instruments and Methods in Physics Research A 581 (2007) 517–521

NUCLEAR INSTRUMENTS & METHODS IN PHYSICS RESEARCH Section A

www.elsevier.com/locate/nima

Gamma-ray imaging with a large micro-TPC and a scintillation camera

K. Hattori[a,*], S. Kabuki[a], H. Kubo[a], S. Kurosawa[a], K. Miuchi[a], T. Nagayoshi[b], H. Nishimura[a], Y. Okada[a], R. Orito[c], H. Sekiya[a], A. Takada[a], A. Takeda[d], T. Tanimori[a], K. Ueno[a]

[a]*Graduate School of Science, Department of Physics, Kyoto University Kitashirakawa, Sakyo, Kyoto 606-8502, Japan*
[b]*Advanced Research Institute for Science and Engineering, Waseda University, 17 Kikui-cho, Shinjuku 162-0044, Tokyo, Japan*
[c]*Graduate School of Science and Technology, Department of Physics, Kobe University, 1-1 Rokkoudai, Nada, Kobe 657-8501, Japan*
[d]*Kamioka Observatory, ICRR, University of Tokyo, 456 Higashi-mozumi, Hida-shi, Gifu 505-1205, Japan*

Available online 7 August 2007

Abstract

We report on the development of a large Compton camera with the full reconstruction of the Compton process based on a prototype. This camera consists of two kinds of detectors. One is a gaseous time projection chamber (micro-TPC) for measuring the energy and the track of a Compton recoil electron. The micro-TPC is based on a μ-PIC and a GEM, which are micro-pattern gas detectors (MPGDs). The size of the micro-TPC was 10 cm × 10 cm × 8 cm in the case of the prototype, and we enlarged it to 23 cm × 28 cm × 15 cm. The other detector part is a NaI (Tl) Anger camera for measuring the scattered gamma-ray. With these informations, we can completely reconstruct a Compton event, and determine the direction of the incident gamma-ray, event by event. We succeeded in reconstructing events of incident 662 keV gamma-rays. The measured angular resolutions of the "angular resolution measure" (ARM) and the "scatter plane deviation" (SPD) were 9.3° and 158° (FWHM), respectively.

PACS: 29.40.Cs; 29.40.Gx

Keywords: Compton imaging; Time projection chamber; MeV gamma-ray imaging

1. Introduction

In spite of the successful all-sky survey using COMPTEL [1] on board the Compton Gamma Ray Observatory (CGRO) satellite, the number of celestial objects found in the MeV gamma-ray band was smaller by an order of magnitude than that found in the GeV band. Thus, a Compton telescope with improved detection sensitivity is desired. Since the direction of a Compton recoil electron was not measured with COMPTEL, the direction of the incident photon could only be reconstructed as a cone. Accordingly, it was difficult to reject large background, thereby limiting the sensitivity. Measuring the direction of the recoil electron reduces the Compton cone to a small segment of the cone, and realizes the strong background rejection [2,3]. To measure both the three-dimensional track and the energy of the recoil electron, we have developed a gaseous time projection chamber (micro-TPC) based on a "micro-pixel chamber" (μ-PIC), which is a pixel-type two-dimensional imaging detector with a pixel pitch of 400 μm [4]. Both the energy and the direction of the scattered gamma-ray are measured using a NaI(Tl) scintillation camera. Through these measurements, the direction and the energy of the incident gamma-ray can be determined event by event.

Our goal is to achieve a sensitivity 10 times as high as that of COMPTEL. To attain this, we first developed a prototype of the Compton camera operating in the 0.1–0.9 MeV range consisting of a 10 cm × 10 cm × 8 cm micro-TPC and a 10 cm × 10 cm × 2.5 cm NaI(Tl) camera [5]. We showed that the direction and the energy of the incident gamma-ray can be determined event by event. Based on the prototype, we developed a larger size

*Corresponding author.
E-mail address: hattori@cr.scphys.kyoto-u.ac.jp (K. Hattori).

0168-9002/$ - see front matter © 2007 Elsevier B.V. All rights reserved.
doi:10.1016/j.nima.2007.08.039

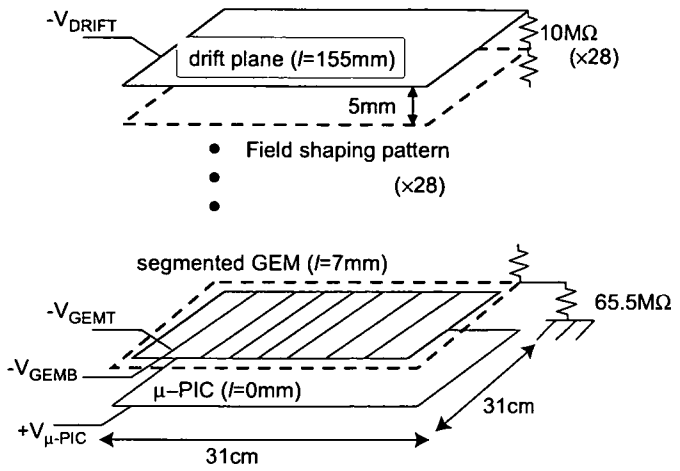

Fig. 1. Schematic representation of the micro-TPC. *l* indicates the vertical dimension.

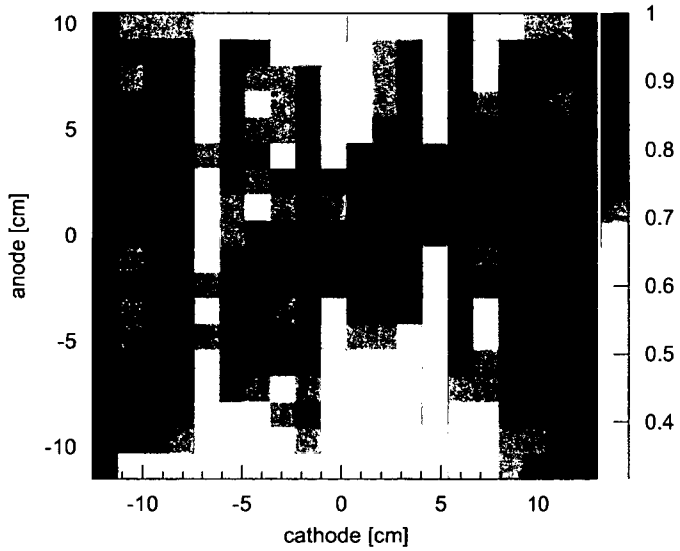

Fig. 2. Gainmap of the micro-TPC. The maximum gain was normalized to 1.

MeV-gamma-ray camera consisting of a 23 cm × 28 cm × 15 cm micro-TPC and a 37 cm × 37 cm × 2.5 cm NaI(Tl) camera. In this paper we present the results of the initial experimental evaluation of the large Compton camera.

2. Large size micro-TPC

We have developed a large size μ-PIC with a detection area of 31 cm × 31 cm [6] for use in the readout of the large size micro-TPC as shown in Fig. 1. The stable gas gain of the large μ-PIC was 2×10^3. However, a gas gain of 2×10^4

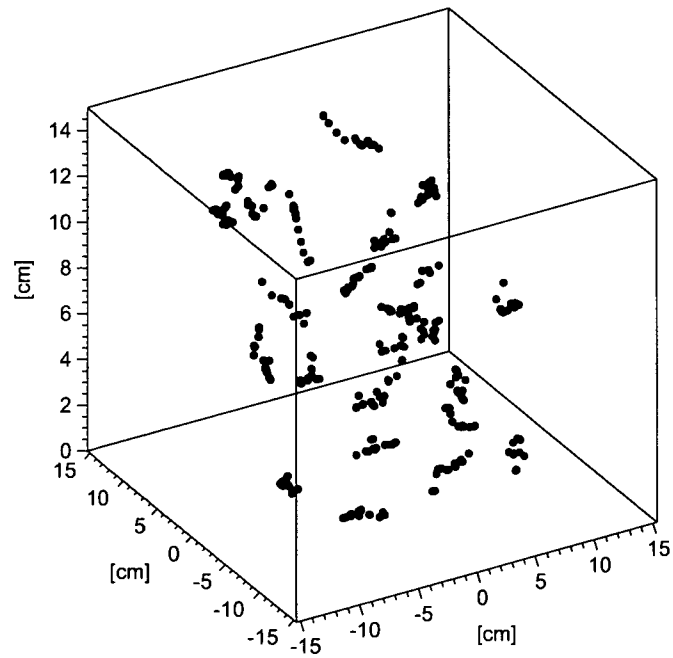

Fig. 4. Tracks of Compton recoil electrons in the micro-TPC irradiated with gamma-rays from the ^{137}Cs source.

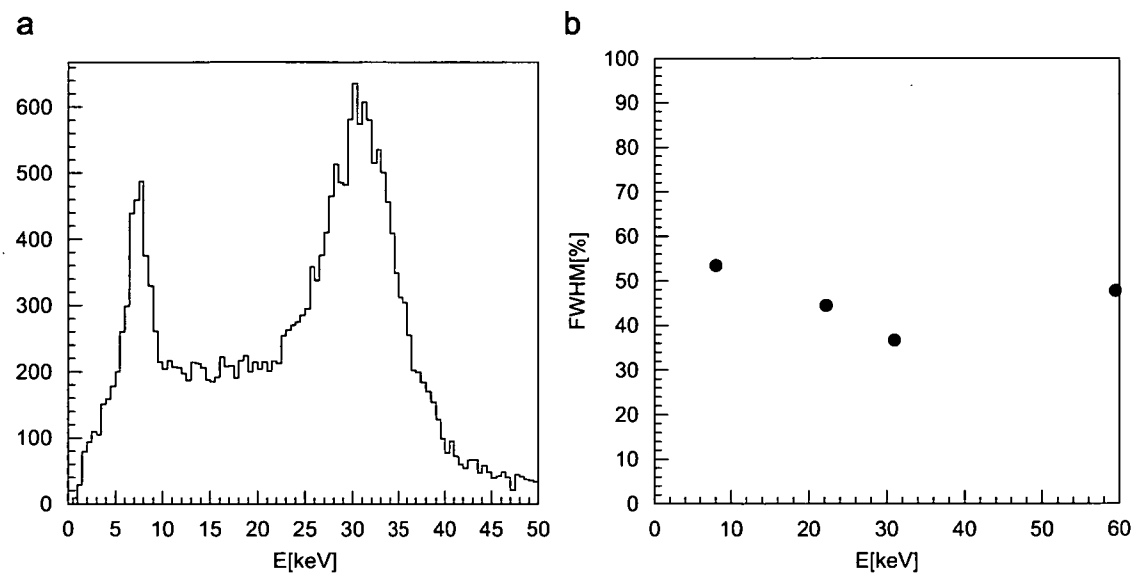

Fig. 3. (a) Spectrum of ^{133}Ba measured with the whole volume of the micro-TPC. (b) Energy resolutions of the micro-TPC.

is required to obtain clear tracks of recoil electrons. Therefore a combination of the μ-PIC and another electron multiplier was necessary. A Gas Electron Multiplier (GEM) [7], manufactured by Scienergy Co. Ltd. in Japan [8], was installed 7 mm above the μ-PIC. The GEM consists of a 50 μm thick kapton foil, and a copper cladding on each side where 70 μm holes are arranged in a hexagonal pattern with 140 μm between the centers. The detection area of the GEM was limited by the size of the material which the company was capable to handle. As a result, the sensitive area of the two-dimensional readout using the μ-PIC and the GEM was 23 cm × 28 cm. The GEM was segmented in eight regions in order to reduce its capacitance, because less capacitance reduces both current and damage caused by discharges. The electric field between the GEM and the μ-PIC was 1.4 kV/cm, and that in the drift region was 0.41 kV/cm. We achieved the stable gas gain of 2×10^4 using the combined system of the μ-PIC and the GEM, and this fulfilled the gas gain requirement.

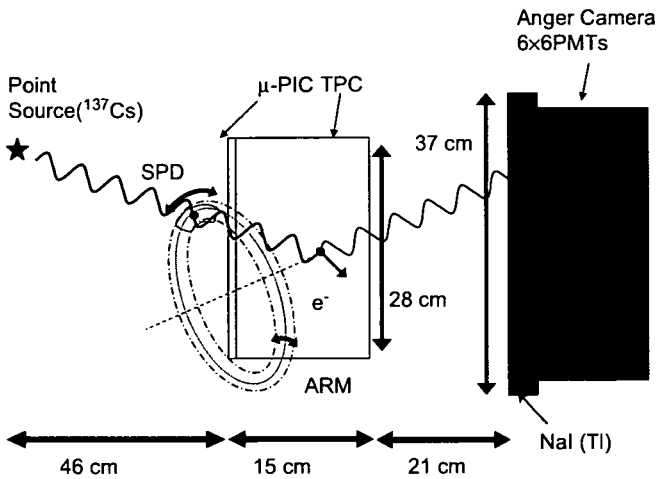

Fig. 5. Schematic representation of the Compton camera.

The micro-TPC was set in an aluminum vessel, the vessel was filled with $Ar-C_2H_6$ (90:10) gas to a pressure of 1 atm and then sealed for the duration of the measurements. The gas gain uniformity of the combined system was 13.9% RMS, as shown in Fig. 2. This was measured using 22.2 keV (^{109}Cd) X-rays at a total gas gain of 1×10^4 (μ-PIC 1.5×10^3, GEM 7). Fig. 3(a) shows a typical spectrum of X-rays obtained by the irradiation with ^{133}Ba. We can see the peak of the direct X-rays at 31 keV and that of the copper fluorescent X-rays at 8.0 keV, generated at the GEM and the μ-PIC by the original X-rays from ^{133}Ba. The energy resolution of the micro-TPC was measured to be 37% FWHM at 31 keV. This depended on the X-ray energy as shown in Fig. 3(b): below 31 keV the energy resolution improved with increasing energy. However, it was worse at 59.5 keV. This might be because of saturation effects in the preamplifiers. The situation is considered to worsen at higher energy, as more charges are presented to the preamplifiers.

In a previous measurement with 31 keV X-rays the energy resolution of the micro-TPC was worse, it was at about 60% FWHM, as described in Ref. [9]. Further modifications in the μ-PIC improved the gas gain uniformity, and therefore the better energy resolution of 37% FWHM was obtained.

The output charges of the 768 + 768 channels are pre-amplified, shaped and discriminated by ASD chips [10]. Using the discriminated signals, the three-dimensional tracks of charged particles are reconstructed. Clear tracks of cosmic muons were observed at a total gas gain of 3.0×10^4 (1.5×10^3 of the μ-PIC, 20 of the GEM). The spatial

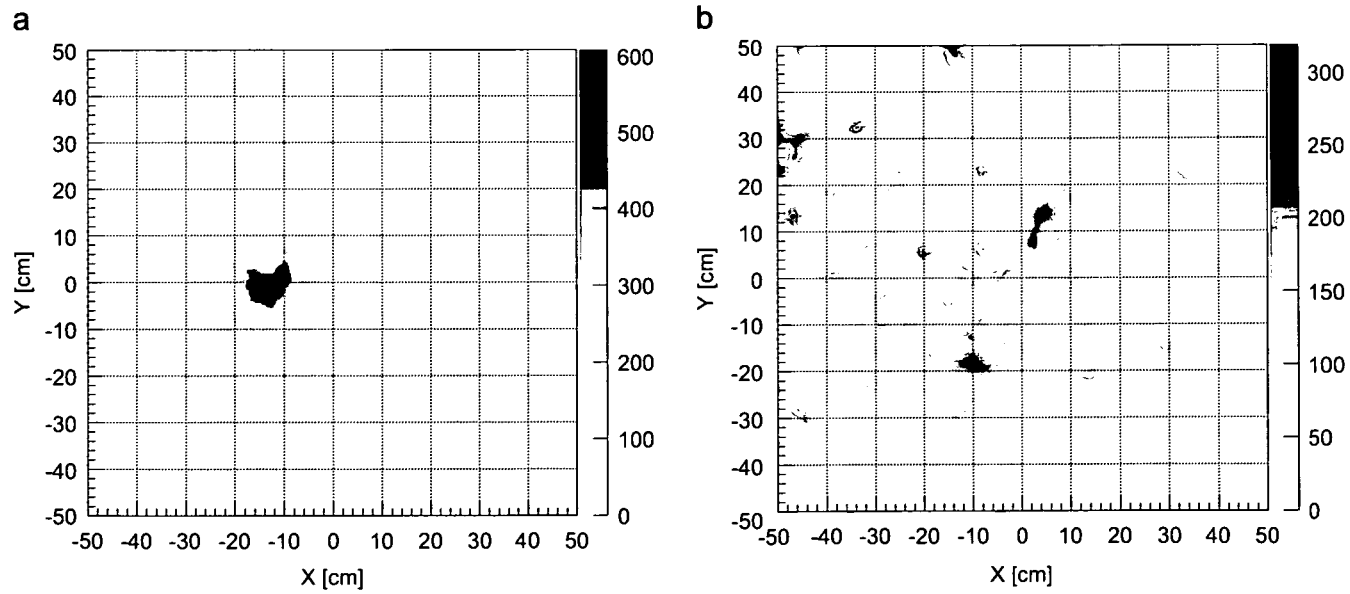

Fig. 6. Reconstructed images of incident gamma-rays from a ^{137}Cs (1 MBq) source. The center of the μ-PIC is (0 cm, 0 cm). (a) The source position is (−14 cm, 0 cm). (b) The positions of two sources are (−10 cm, −20 cm) and (5 cm, 15 cm), respectively.

resolution of the muon tracks was $\sqrt{0.56^2 + 0.31^2 z}$ (mm), where z was the drift length. Fig. 4 shows typical recoil electron tracks obtained by irradiating with ^{137}Cs. We find that the electrons were multi-scattered in the gas.

3. Large size Compton camera

Here, we describe the performance of the large size Compton camera. As shown in Fig. 5, it is built using the micro-TPC and the NaI(Tl) Anger camera. The size of the NaI(Tl) camera was 37 cm × 37 cm × 2.5 cm. The details of the scintillation detector are described elsewhere [11].

The micro-TPC was operated at a gas gain of 2×10^4 (2×10^3 of the μ-PIC, 10 of the GEM). The Compton camera was irradiated with 662 keV gamma-rays by a ^{137}Cs source from a distance of approximately 46 cm, and the reconstructed image is shown in Fig. 6(a). The ^{137}Cs source position was (−14 cm, 0 cm), the center of the μ-PIC was (0 cm, 0 cm). The reconstructed directions of the detected photons were concentrated on the position of the source. Fig. 6(b) shows the reconstructed images of two ^{137}Cs point sources, and we succeeded in separating them.

The angular resolution of advanced Compton imaging is defined by two angle parameters as shown in Fig. 7. One is the "angular resolution measure" (ARM) related to the angle between the scattered gamma-ray and the recoiled electron. This can be obtained in two ways, from kinematics and from geometry. ARM is the difference between these values. The other parameter is the "scatter plane deviation" (SPD), which is the determination accuracy of the plane formed by the scattered gamma-ray and the recoiled electron. Fig. 8 shows the distributions of ARM and SPD obtained for the data corresponding to Fig. 6(a), and the FWHM resolutions of ARM and SPD are 9.3° and 158°, respectively. In the case of the prototype with a 10 cm × 10 cm × 8 cm micro-TPC, the FWHM resolutions of ARM and SPD were typically 9° and 90°, respectively. Therefore, the ARMs of the large Compton camera and of the prototype were almost the same; however, the SPD of the large camera was greater. The SPD is determined by the accuracy of measuring the directions of the recoil electrons. If the signal-to-noise ratio of the large micro-TPC is improved, this accuracy also improves because more precise measurements for the tracks of the recoil electrons can be obtained. In the case of the prototype, the accuracy was better because the signal-to-noise ratio was better.

For the 662 keV gamma-rays, the measured detection efficiency was 2×10^{-6}. The low gamma-ray detection efficiency was caused mainly by the low detection efficiency of high-energy (>100 keV) recoil electrons. However, the volume of the micro-TPC is large enough for even 300 keV electrons to transfer all the energy to the gas in the micro-TPC. It is thought that there are two reasons for the low detection efficiency of the high-energy recoil electrons. One is the small solid angle coverage of the scintillation detector, placed at 21 cm distance from the micro-TPC as shown in Fig. 5. This means that it detected mainly low-angle scattered gamma-rays, and the majority of the Compton-scattered gamma-rays escaped the detection. The low-angle scattered gamma-rays transfer only low energy to the recoil electrons. Correspondingly, high-energy recoil electrons in the micro-TPC do not coincide with hits in the scintillation detector. This will be improved by enlarging the solid angle coverage of the scintillation detector.

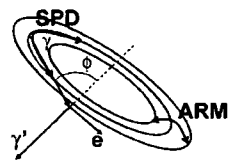

Fig. 7. The schematic view of ARM and SPD.

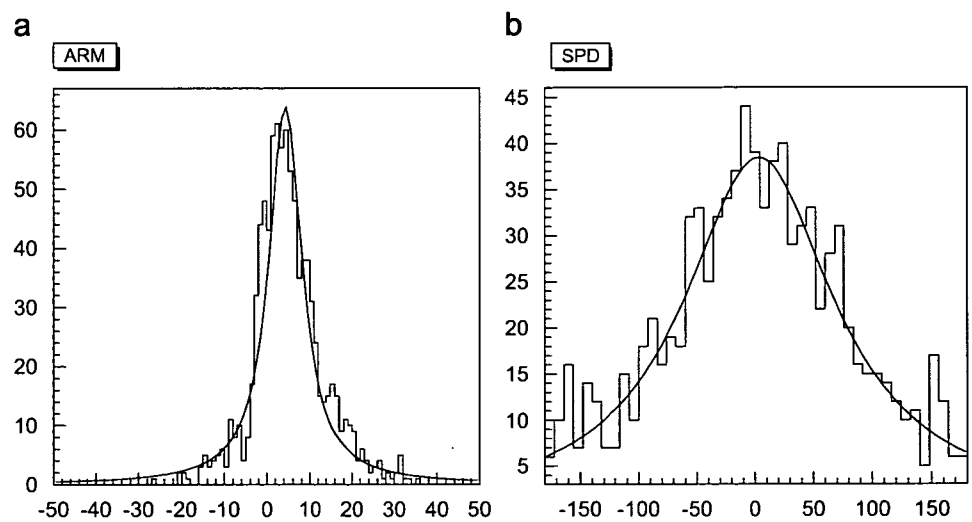

Fig. 8. (a) and (b) show the distributions of ARM and SPD for 662 keV gamma-rays, respectively. The solid lines are the best-fit Lorentzian.

The second reason is ascribed to the saturation effects in the preamplifiers, as described in the previous section. They cause a deteriorated energy resolution of the recoil electrons at higher energies, what also leads to a low gamma-ray detection efficiency due to a background rejection algorithm. This is based on a consistency check where the alpha-angle (the angle between the recoil electron and the scattered gamma-ray), as derived by kinematics from the energies of the recoil electron and of the scattered gamma-ray, is compared to the angle which is geometrically deduced from the directions of the recoil electron and of the scattered gamma-ray [2]. Compton events with a large difference of the two angles were rejected. Consequently, we have developed new ASD chips with a wider dynamic range to avoid the saturation in the preamplifiers.

4. Conclusion

We have developed a micro-TPC, based on the μ-PIC with a detection area of 30 cm × 30 cm and a GEM with a detection area of 23 cm × 28 cm, the drift length was 15 cm. The combination of the μ-PIC and a GEM realized stable operation of the chamber at a gas gain of 2×10^4, and this was adequate to obtain tracks of minimum ionizing particles and thus of recoil electrons. Then, the performance of the Compton camera (consisting of the micro-TPC and the Anger camera) was investigated by irradiating with 662 keV gamma-rays from a ^{137}Cs source. We succeeded in reconstructing recoil electrons recorded with the micro-TPC and we obtained fine images of different point sources.

References

[1] V. Schoenfelder, et al., Astrophys. J. Suppl. Ser. 86 (1993) 657.
[2] R. Orito, et al., Nucl. Instr. and Meth. A 513 (2003) 408.
[3] T. Tanimori, et al., New Astron. Rev. 517 (2004) 241.
[4] A. Ochi, et al., Nucl. Instr. and Meth. A 471 (2001) 264.
[5] T. Tanimori, et al., New Astron. Rev. 48 (2004) 263.
[6] A. Takada, et al., Nucl. Instr. and Meth. A 573 (2007) 195.
[7] F. Sauli, Nucl. Instr. and Meth. A 386 (1997) 531.
[8] M. Inuzuka, et al., Nucl. Instr. and Meth. A 525 (2004) 529.
[9] K. Miuchi, et al., Nucl. Instr. and Meth. A 576 (2007) 43.
[10] H. Kubo, et al., Nucl. Instr. and Meth. A 513 (2003) 94.
[11] R. Orito, et al., 2005 IEEE Conference Record, vol. 1, 2005, pp. 443–447.

資料(8)

Available online at www.sciencedirect.com
ScienceDirect
ELSEVIER
Nuclear Instruments and Methods in Physics Research A 581 (2007) 110–114
NUCLEAR INSTRUMENTS & METHODS IN PHYSICS RESEARCH Section A
www.elsevier.com/locate/nima

Response of a Micro Pixel Chamber to heavy ions with the energy of several hundreds of MeV/n

Tsutomu Nagayoshi[a,*], Tadayoshi Doke[a,d], Yasunobu Fujita[a], Kaori Hattori[b], Koji Ishida[a], Jun Kikuchi[a], Hisashi Kitamura[e], Tatsuto Komiyama[d], Hidetoshi Kubo[b], Haruhisa Matsumoto[d], Kentaro Miuchi[b], Hironobu Nishimura[b], Kiwamu Saito[c], Shin-ichi Sasaki[c], Hiroyuki Sekiya[b], Atsushi Takada[b], Toru Tanimori[b], Kazuhiro Terasawa[a,d], Hiroko Tawara[c], Yukio Uchihori[e], Kazuki Ueno[b]

[a]*Waseda University, 17 Kikuicho, Shinjuku-ku, Tokyo 162-0044, Japan*
[b]*Kyoto University, Kitashirakawa-oiwakecho, Sakyo-ku, Kyoto 606-8502, Japan*
[c]*High-Energy Accelerator Research Organization (KEK), 1-1 Oho, Tsukuba, Ibaraki 305-0801, Japan*
[d]*Japan Aerospace Exploration Agency (JAXA) 2-1-1 Sengen, Tsukuba Ibaraki 305-8505, Japan*
[e]*National Institute of Radiological Sciences (NIRS), 4-9-1 Anagawa, Inage-ku, Chiba 263-8555, Japan*

Available online 26 July 2007

Abstract

Beam tests were performed for a Micro Pixel Chamber (μ-PIC) with a detection volume of $10 \times 10 \times 10\,cm^3$ to investigate the response to heavy ions. The three-dimensional tracks of carbon, silicon, and iron beams were successfully observed and their track lengths were measured. Additionally, Linear Energy Transfer (LET) distributions of each ion were obtained, and the mean LET values were consistent with the theoretical calculation of mass stopping power within an error of ~10%. This detector is a candidate for an ideal dosimeter in space.

PACS: 29.40.Cs; 29.40.Gx

Keywords: Gaseous detector; Micro-Pattern detector; Position sensitive; TEPC; LET; Heavy ions

1. Introduction

We have been developing the position sensitive gaseous detector named "Micro Pixel Chamber (μ-PIC)" [1], which is categorized as a micro-pattern gas detector. The μ-PIC consists of a double-sided printed circuit board (PCB) with pixel-like electrodes. The anode and cathode strip electrodes are orthogonally arranged with a pitch of 400 μm on both sides of the 100 μm thick polyimide insulation layer. Each cathode strip has 260 μm diameter openings with a pitch of 400 μm. Pixel-like anode electrodes of 60 μm are also formed at the center of each cathode hole penetrating the insulator. Our μ-PIC has 256 anode and 256 cathode strips, and the detection area is $10 \times 10\,cm^2$. The μ-PIC has the following features:

(1) no charging-up of positive ions on the insulator surface,
(2) little fluctuation of gas gain in whole detection area (<4% RMS for $10 \times 10\,cm^2$ detection area),
(3) two-dimensional fine position resolution (120 μm RMS),
(4) high gas gain (~7000) without any other additional gas multiplication devices,
(5) mass production capability.

The main use of the μ-PIC is the 3D imaging of charged particles. For this purpose, μ-PIC is operated as a readout of a Time Projection Chamber (TPC) named the "μ-TPC" [2], which has an $11 \times 11 \times 10\,cm^3$ drift space. Fig. 1 shows

*Corresponding author. Tel./fax: +81 3 3203 4379.
E-mail address: nagayosi@kurenai.waseda.jp (T. Nagayoshi).

0168-9002/$ - see front matter © 2007 Elsevier B.V. All rights reserved.
doi:10.1016/j.nima.2007.07.040

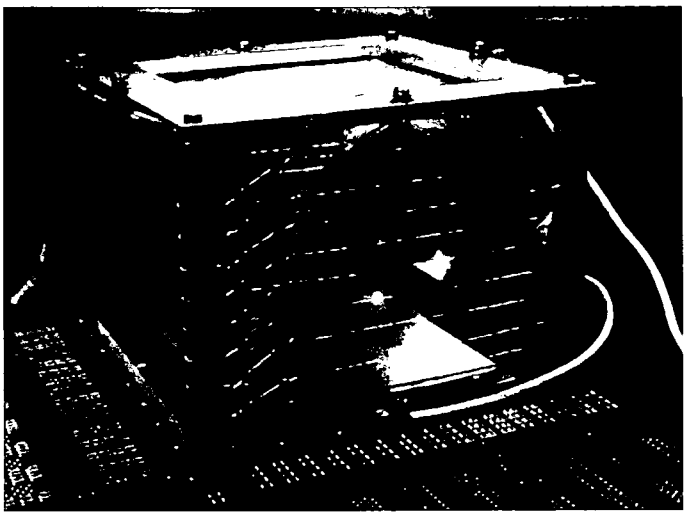

Fig. 1. Photograph of a μ-PIC with an 11 × 11 × 10 cm³ drift cage.

a photograph of the μ-TPC. The 0.5 mm diameter field wires are arranged with a pitch of 1 cm. Resistances of 10 MΩ are connected between two adjacent field wires. Ionization electrons drift to the plane of μ-PIC and the two-dimensional position is detected by anode and cathode electrodes. The z-position is then measured from the information of known drift velocity of electrons and the drift time. According to former experiments with proton tracks of ~1 GeV, the 3D position resolution of less than 300 μm was achieved.

Originally, we have been developing the μ-TPC for the application of gamma-ray imaging onboard a satellite, based on tracking of Compton scattered electrons [3]. Because the typical energy of a scattered electron is 1 MeV—the MIP energy region—, high gas gain operation ($>10^4$) is needed. Heavy ions in cosmic-rays might be a serious problem for the detector. Ionization in the detector due to cosmic-ray particles creates an enormous number of electron–ion pairs, which might cause discharges [4]. Therefore, the influence of the heavy ion irradiation to the μ-TPC should be studied to ensure stable operation of the detector in a space environment.

When astronauts work in a space environment like the International Space Station (ISS) or manned exploration to the Moon or Mars, exposure to cosmic radiation including extremely large solar flares sometimes gives the large risk to the crew. The μ-TPC is a candidate of an ideal dosimeter in space as a LET spectrometer. The details for space dosimetry are described elsewhere [5]. In this case, a gas gain of 100 to 1000 is needed to measure the LET of heavy ions.

For these purposes, it is necessary to evaluate the response of the μ-TPC to heavy ions. We performed irradiation tests for a μ-TPC using the heavy ion accelerator at National Institute of Radiological Sciences (NIRS) in Japan. In this paper, we describe the heavy ion irradiation test and discuss the response of the μ-TPC.

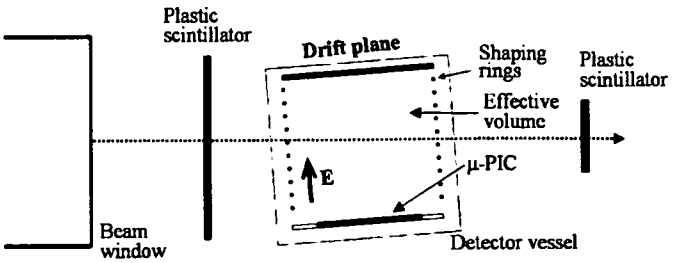

Fig. 2. Set-up of the μ-TPC at the HIMAC beamline. The trigger scintillators are also shown. The beam penetrates this set-up horizontally.

2. Heavy ion irradiation experiment at HIMAC

The beam experiments were carried out at the Heavy-Ion Medical Accelerator in Chiba (HIMAC) of NIRS. The beam energies were 400 MeV/n for carbon ions, 800 MeV/n for silicon, and 500 MeV/n for iron ions, because the typical energy of heavy ions in cosmic ray is 100 MeV to 1 GeV [6].

The experiment setup at the beamline is shown in Fig. 2. The detector was inclined at 5° against the horizontal in order to evaluate the Z direction of the beam tracks. One scintillation counter was placed in front of and one behind the μ-TPC. The data acquisition system was triggered by coincidental hits from both scintillators. These triggering signals are produced when a particle passes through the whole detector system.

The drift volume was filled with a gas mixture of the Ar/C_2H_6(90/10) at 1 bar, and a drift voltage of 2000 V was applied on the top of the drift cage. The corresponding drift electric field was 0.2 kV/cm. The drift velocity of electrons in the gas mixture was 4.5 cm/μs at the drift electric field [7].

An ^{241}Am α source was deposited on the top plane of the drift cage for an energy calibration. To restrict the intensity of the irradiation the α source was placed 5 mm above the drift plane and collimated by a 2 mm diameter hole at the center of the drift plane. The total energy deposit of α particles in the detection volume of the μ-TPC was effectively 5 MeV.

The ionization electrons drift to the μ-PIC plane along the lines of electric force and are multiplied in the neighborhood of the anode pixels. The strip electrodes are connected to the Amplifier Shaper Discriminator (ASD) chips of a time constant of 80 ns [8]. The digital signals from the ASD chips are fed to the front-end position encoding module (PEM) based on five Field Programmable Gate Arrays (FPGAs). The hit positions of the electrodes are encoded as a three-dimensional image. Thus the three-dimensional track is reconstructed using the clock information together with the X- and Y-information. To analyze the pulse shape from the anode, all analog signals from the ASDs are summed up into one channel which is fed to a 100 MHz flash ADC (FADC). The energy deposit of each incident particle is

calculated from the integrated wave form using the calibration data.

3. Results and discussion

The μ-PIC was stable during operation at a gas gain of ~100 even for an iron beam which had the highest energy deposit. There was no gas gain variation between before and after the irradiation.

The beam profiles for carbon, silicon, and iron ions have similar shapes with a 10 mm diameter. Fig. 3 shows the detected three-dimensional tracks for a silicon beam. This is composed of the superposed images of 50 tracks. The cross-sectional views for three beam profiles are given in Fig. 4 with their projections to the horizontal and the vertical axes. In this figure, the absolute value in the x-axis is insignificant and only the width of the distribution can be evaluated. The shapes of the beam profiles are properly reconstructed, compared with the beam profile monitor just before the end window of the beam line. The width of the histogram for each projection was consistent with the size of beam profile.

The reconstructed tracks were shown as a sequence of points produced by a timing of the clock frequency in the data acquisition system. Each sequence of points was fitted by a three-dimensional linear function. The track length is defined as the length along this function from an end to another end in the effective drift region. The distribution of the track lengths are shown in Fig. 5. The difference in the

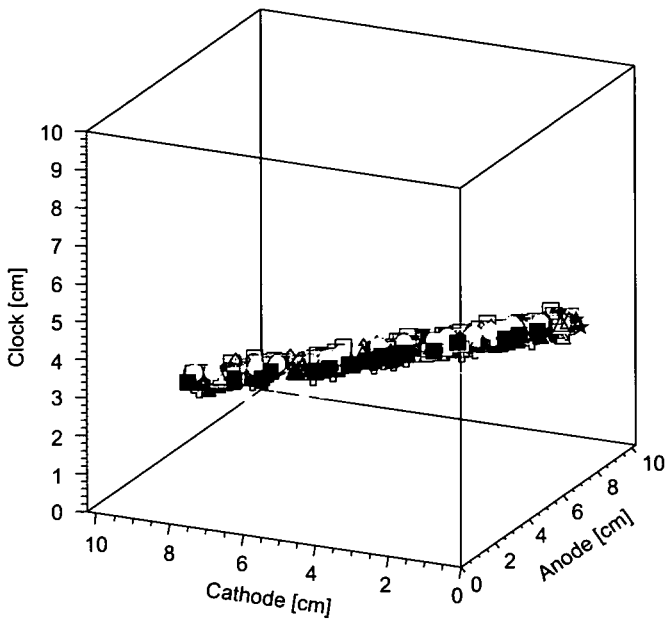

Fig. 3. Reconstructed three-dimensional image of Si tracks in the Ar/ethane (90/10) gas. One hundred tracks are superimposed in the figure.

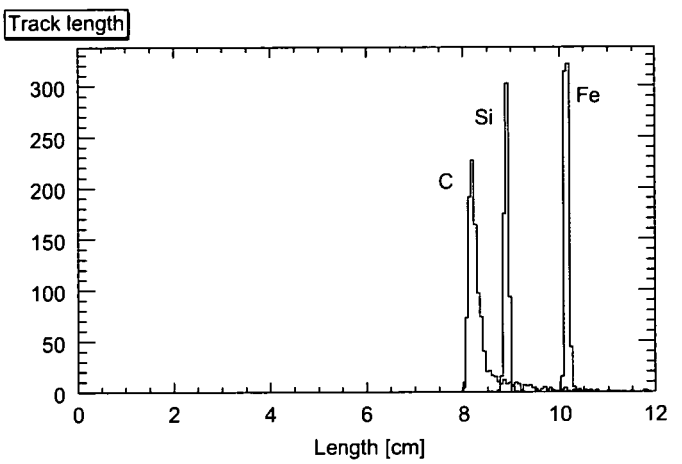

Fig. 5. Distribution of each track length for carbon, silicon, and iron beams.

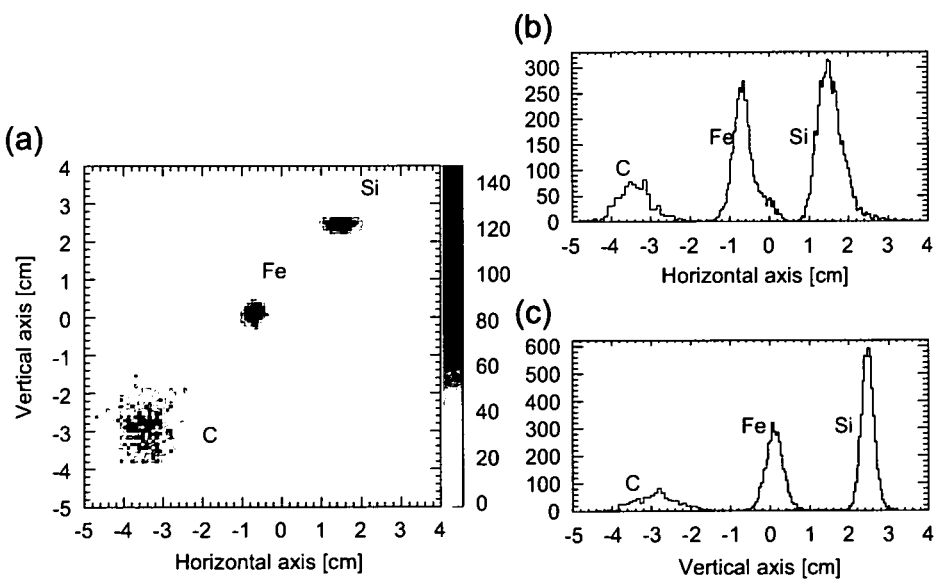

Fig. 4. Reconstructed beam profiles for carbon, silicon, and iron ions (a) and their projections to horizontal (b) and vertical axes (c).

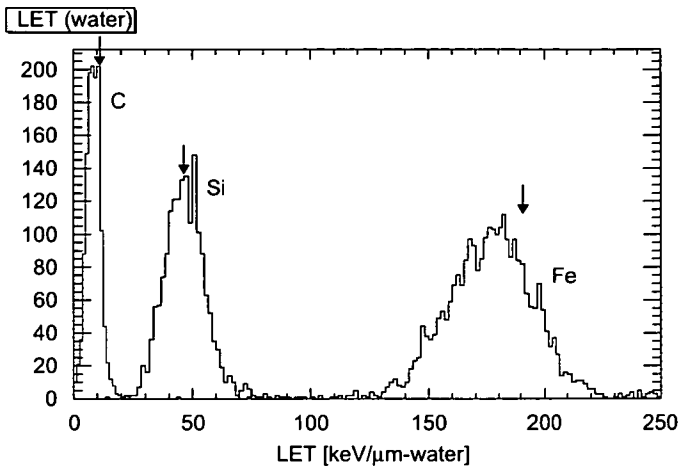

Fig. 6. LET distribution of carbon, silicon, and iron ion tracks. The arrows shows the results of theoretical calculation.

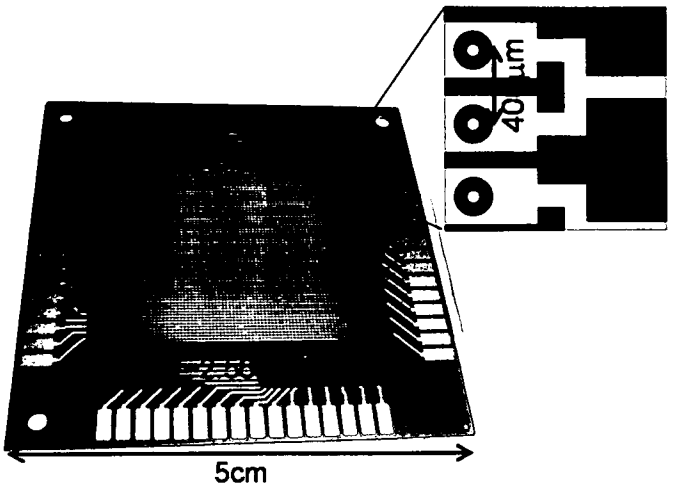

Fig. 7. Photograph of a μ-PIC with the size of $2.6 \times 2.6\,cm^2$ together with the schematic drawing of the electrodes.

track length is consistent with the setup of each experiment. In this case, a dead layer existed in the effective volume. Therefore, the track length was less than 11 cm. The small tail for carbon ions is due to some noise events affecting the fitting process. Taking these reasons into consideration, these results are satisfactory.

We need to measure the LET of each particle for space dosimetry; in particular, the LET in water is essential. The distribution of energy deposits of each ion is also obtained as well as the track length [9]. LET for each event was calculated by energy deposit and track length. Fig. 6 shows the LET distributions for three kinds of ions. The theoretical values calculated by SRIM program [10] are also shown as arrows in this figure. The following equations were used to obtain the LET for water from that for Ar/ethane gas.

$$LET_{water}\ [keV/\mu m] = LET_{Ar/ethane} \times 1.28 \times 1.00/(1.62 \times 10^{-3}) \quad (1)$$

$$LET_{Ar/ethane} = (\text{energy deposit})/(\text{track length})\ [keV/\mu m]. \quad (2)$$

Here, LET_{water} is the LET for water and $LET_{Ar/ethane}$ is that for the Ar/ethane (90/10) gas mixture. The conversion factor corresponding to the ratio of the mass stopping power of water for relativistic particles to that of Ar/ethane is 1.28. The density of water is 1.00 and that of 1 bar Ar/ethane is 1.62×10^{-3}. The difference between theoretical and experimental LET values of carbon was about 10%. The mean LET value for each distribution of silicon and iron was consistent with the theoretical values of the mass stopping power within an error of about 5%.

4. Summary and future prospect

Irradiation tests of a μ-TPC with an effective volume of $10 \times 10 \times 10\,cm^3$ were performed using heavy ion beams at HIMAC of NIRS in Japan. The μ-PIC was stably operated for the heavy ion irradiation. Three-dimensional tracks of carbon, silicon, and iron ions were successfully measured. Their track lengths and energy deposits in the detector were also measured. Finally, we evaluated the LET value for each particle and found the values to be consistent with the theoretical calculation within an error of 10%. This is essential for the LET spectrometer in space. In this paper, we established the principle of the cosmic-ray dosimeter based on the μ-PIC.

For utilization in space, the robustness of the μ-PIC for heavy ion irradiation has to be checked. The response of the μ-PIC to heavy particles is important for high gas gain ($> 10^4$) operations like cosmic MeV gamma-ray observation. A dosimeter for space applications must be small so it can be installed on a spacecraft. A smaller size μ-PIC has recently been manufactured in order to develop a new space dosimeter. Fig. 7 presents a photograph of a μ-PIC with an effective area of $2.6 \times 2.6\,cm^2$. In the new design, the 400 μm pitch electrodes are connected with the adjacent strips as shown in Fig. 7, and the net electrode pitch is 800 μm. The position resolution obtained from the pitch is adequate for space dosimetry based on the results of Real-time Radiation Monitoring Device-III (RRMD-III) [11]. Furthermore, the detector should be made from tissue equivalent materials. In the near future, we will make the dosimeter with a tissue equivalent wall and a tissue equivalent gas.

Acknowledgments

This study is being carried out as a part of "Ground Research Announcement for Space Utilization", promoted by the Japan Space Forum. T. Nagayoshi is supported by Research Fellowships of Japan Society for the Promotion of Science for Young Scientists.

References

[1] A. Ochi, et al., Nucl. Instr. and Meth. A 471 (2001) 264;
T. Nagayoshi, et al., Nucl. Instr. and Meth. A 513 (2003) 277;
T. Nagayoshi, et al., Nucl. Instr. and Meth. A 525 (2004) 20.

[2] H. Kubo, et al., Nucl. Instr. and Meth. A 413 (2003) 94;
K. Miuchi, et al., Nucl. Instr. and Meth. A 535 (2004) 236.
[3] R. Orito, et al., Nucl. Instr. and Meth. A 513 (2003) 408;
A. Takada, et al., Nucl. Instr. and Meth. A 546 (2005) 258.
[4] A. Bressan, et al., Nucl. Instr. and Meth. A 424 (1999) 321.
[5] K. Terasawa, et al, in: Proceedings of the 19th Workshop on Radiation Detectors and their Uses, KEK Proceedings, vol. 2005-12, 2005, p. 63.
[6] J.A. Simpson, Ann. Rev. Nucl. Part. Sci. 33 (1983) 330.
[7] The MIT LNS Drift Gases R&D Experiment, (http://cyclo.mit.edu/drift/www/).
[8] R. Orito, et al., IEEE Trans. Nucl. Sci. 51 (2004) 1337.
[9] T. Nagayoshi, in: Proceedings of the 20th Workshop on Radiation Detectors and Their Uses, KEK Proceedings, vol. 2006-7, 2006, p. 1.
[10] J.F. Ziegler, J.P. Biersack, U. Littmark, SRIM-The Stopping and Range of Ions in Matter, Pergamon, New York, 1985.
[11] T. Doke, et al., Radiat. Meas. 33 (2001) 373.

資料(9)

Available online at www.sciencedirect.com
ScienceDirect
Nuclear Instruments and Methods in Physics Research A 580 (2007) 1031–1035
NUCLEAR INSTRUMENTS & METHODS IN PHYSICS RESEARCH Section A
www.elsevier.com/locate/nima

Development of Electron Tracking Compton Camera using micro pixel gas chamber for medical imaging

Shigeto Kabuki[a], Kaori Hattori[a], Ryota Kohara[b], Etsuo Kunieda[c], Atsushi Kubo[c], Hidetoshi Kubo[a], Kentaro Miuchi[a], Tadaki Nakahara[c], Tsutomu Nagayoshi[a], Hironobu Nishimura[a], Yoko Okada[a], Reiko Orito[a], Hiroyuki Sekiya[a], Takashi Shirahata[b], Atsushi Takada[a], Toru Tanimori[a,*], Kazuki Ueno[a]

[a]*Department of Physics, Faculty of Science, Kyoto University, Sakyo-ku, Kyoto 606-8502, Japan*
[b]*Hitachi Medical Corporation, Kashiwa, Chiba 277-0804, Japan*
[c]*Department of Radiography, Keio University, Shinjuku-ku, Tokyo 160-8582, Japan*

Available online 10 July 2007

Abstract

We have developed the Electron Tracking Compton Camera (ETCC) with reconstructing the 3-D tracks of the scattered electron in Compton process for both sub-MeV and MeV gamma rays. By measuring both the directions and energies of not only the recoil gamma ray but also the scattered electron, the direction of the incident gamma ray is determined for each individual photon. Furthermore, a residual measured angle between the recoil electron and scattered gamma ray is quite powerful for the kinematical background rejection. For the 3-D tracking of the electrons, the Micro Time Projection Chamber (μ-TPC) was developed using a new type of the micro pattern gas detector. The ETCC consists of this μ-TPC ($10 \times 10 \times 8\,cm^3$) and the $6 \times 6 \times 13\,mm^3$ GSO crystal pixel arrays with a flat panel photo-multiplier surrounding the μ-TPC for detecting recoil gamma rays. The ETCC provided the angular resolution of 6.6° (FWHM) at 364 keV of ^{131}I. A mobile ETCC for medical imaging, which is fabricated in a 1 m cubic box, has been operated since October 2005. Here, we present the imaging results for the line sources and the phantom of human thyroid gland using 364 keV gamma rays of ^{131}I.

PACS: 13.60.Fz; 29.40.Gx; 87.58.–b; 95.55.Ka

Keywords: Compton camera; Nuclear medicine imaging; Micro pattern gaseous detector; TPC

1. Introduction

We have realized both full ray tracing and the background rejection for MeV and sub-MeV gamma ray imaging by detecting the direction of the scatted electron in Compton process [1–3]. Although the track of the scattered electron was proposed to be useful for higher energy (>2 MeV) gamma ray in the Compton camera based on silicon strip detectors [4–8], multiple scatterings in dense matter intrinsically prevent from obtaining a sufficient angular resolution of it in those energy regions. Hence, a gas-tracking device looks a unique useful detector to catch such a fine track. By measuring both the directions and energies of a recoil gamma ray and a recoil electron in the gas detector as shown in Figs. 1a, the direction of the incident gamma ray can be definitely determined for each Compton scattering. Furthermore, a residual measured angle between the scattered electron and the recoil gamma ray (hereafter, we say α angle) is used for the kinematical background-rejection. This α angle is also calculated from the measured hit positions and energy deposits, and used for the kinematical constraint. Thus, a full ray-tracing method surely provides gamma-ray images of higher quality with less radiation dose. As well known, the detection efficiency of the gas detector is low, but it provides both a large detection volume and an easy handling of signals due to the high gain of it. A simulation

*Corresponding author. Tel.: +81 75 753 3858; fax: +81 75 753 3799.
E-mail address: tanimori@cr.scphys.kyoto-u.ac.jp (T. Tanimori).

0168-9002/$ - see front matter © 2007 Elsevier B.V. All rights reserved.
doi:10.1016/j.nima.2007.06.098

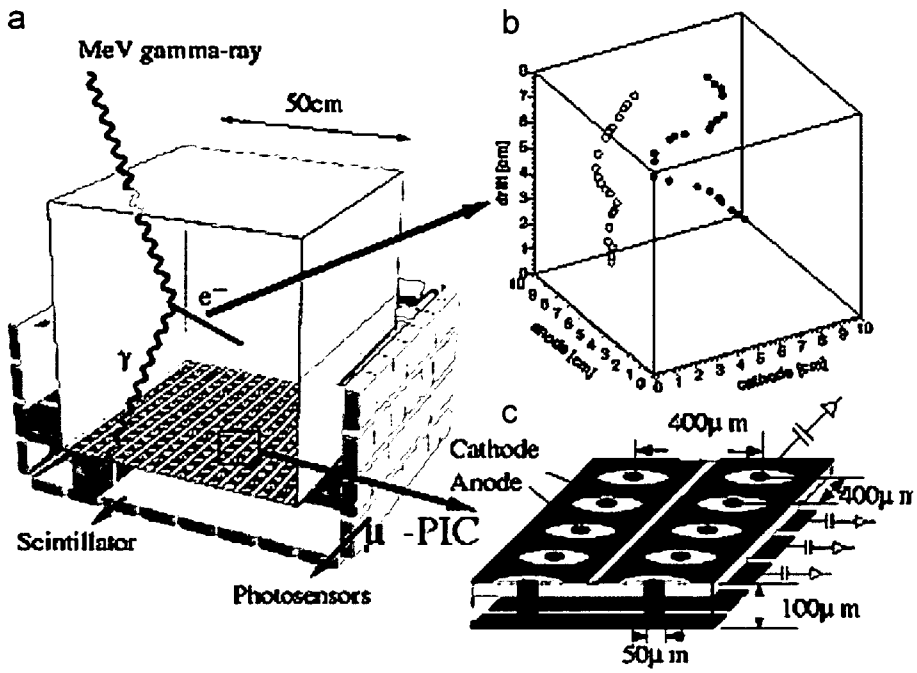

Fig. 1. (a) Conceptual structure of Electron Tracking Compton Camera (ETCC). (b) Typical tracks of electrons from β-decay detected by the μ-TPC. (c) Schematic structure of μ-PIC.

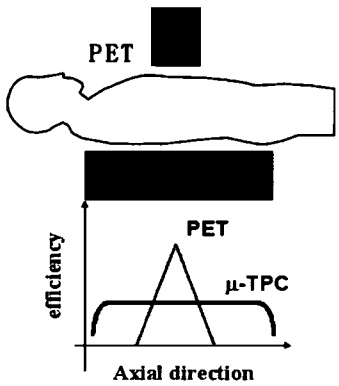

Fig. 2. Schematic comparison of the efficiencies of PET and ETCC along the axial direction of a human body.

study indicates that a $30 \times 30 \times 30\,cm^3$ gas detector with Xe or CF_4 gas pressured by several times atmosphere provides the detection efficiency of a few percent for 500 keV gamma rays, which is better than the typical efficiency of SPECT. Also, such a large volume detector gives a flat efficiency and position resolution as shown in Fig. 2. On the other hand, those of Positron Emission Tomography (PET) are quite good at the center, but linearly worse from the center. Compton camera generally have a wide field of view of 2–4 sr, which covers a large area by ~4 times of the detector size. For the $30 \times 30\,cm^2$ gas detector, its detection area covers the whole body. Thus, a large-area ETCC will surely provide us to new benefits even for the use of radio pharmaceutical which are now used for SPECT and PET.

2. Instrument and imaging performance

In order to realize such an ETCC, we developed the Micro Time Projection Chamber (μ-TPC) for the 3-D tracking of the recoil electrons [1–3]. Typical reconstructed tracks of the low-energy electrons in Compton scattering are shown in Fig. 1b. The μ-TPC consists of a new type of the gaseous proportional two-dimensional wireless position-sensitive detector, or a Micro Pixel Gas Chamber (μ-PIC) [9,10] as shown in Fig. 1c, and a drift volume. The prototype camera consisted of the $10 \times 10 \times 8\,cm^3$ μ-TPC with an argon–ethane gas mixture (9:1) and the Anger camera with a large $30 \times 30 \times 1.5\,cm^3$ NaI(Tl) single scintillator and a 6 × 6 2-in. photo-multiplier array for detecting the scattered gamma rays [11]. For this prototype, the angular resolutions of 12° and 34° (FWHM) for Angular Resolution Measure (AMP) and Scatter Plane Deviation (SPD) were obtained for 662 keV gamma rays when the energy of the incident gamma ray was used as a known parameter [11]. In 2005, we improved this detector as follows; the uses of GEM developed by Sauli et al. [12] as an intermediate electron multiplier above the μ-PIC and $6 \times 6 \times 13\,mm^3$ GSO crystal pixel arrays with a flat panel photo-multiplier surrounding the base and side of the μ-TPC instead of the Anger camera [13–15]. By these improvements, we achieved a stable operation of the μ-TPC with a high gain of >20,000 (μ-PIC:2000, GEM:10) during 1 year, and obtained the energy resolution of the μ-TPC with ~20% at 22.2 keV. In addition, good energy and position resolutions of GSO scintillation array were obtained to be ~3 mm and 9% at 662 keV (FWHM), respectively. Then, combined energy resolution of the

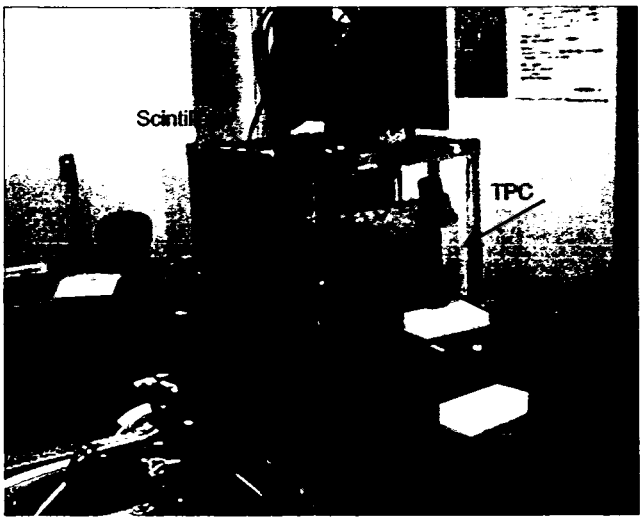

Fig. 3. Photograph of the mobile ETCC. All detectors, electronics, and computers are installed in the wagon.

ETCC for gamma rays was obtained 15% at 662 keV (FWHM). Using this improved ETCC, we obtained an ARM resolution of ~7° at 662 keV (FWHM) with measuring the total energy of the incident gamma ray, of which details are reported in Ref. [15]. Based on this improved ETCC, we have developed a mobile Compton camera fabricated within a 1 m cubic box as shown in Fig. 3 [15]. The angular resolutions of ARM and SPD at 364 keV gamma rays of ^{131}I were improved from 12° and 100° to 6.6° and 77° due to the improvement of the electron reconstruction. We have measured simultaneously the images of the two different energy gamma-ray sources (^{133}Ba: 356 keV and ^{137}Cs: 662 keV) as shown in Fig. 4, where two images are obviously distinguished by the energy spectrum. This is a unique ability expected mainly for the Compton camera in medical use. In Ref. [15], similar images using the point sources of ^{137}Cs: 662 keV and ^{133}Mn: 853 keV were already presented. In this time,

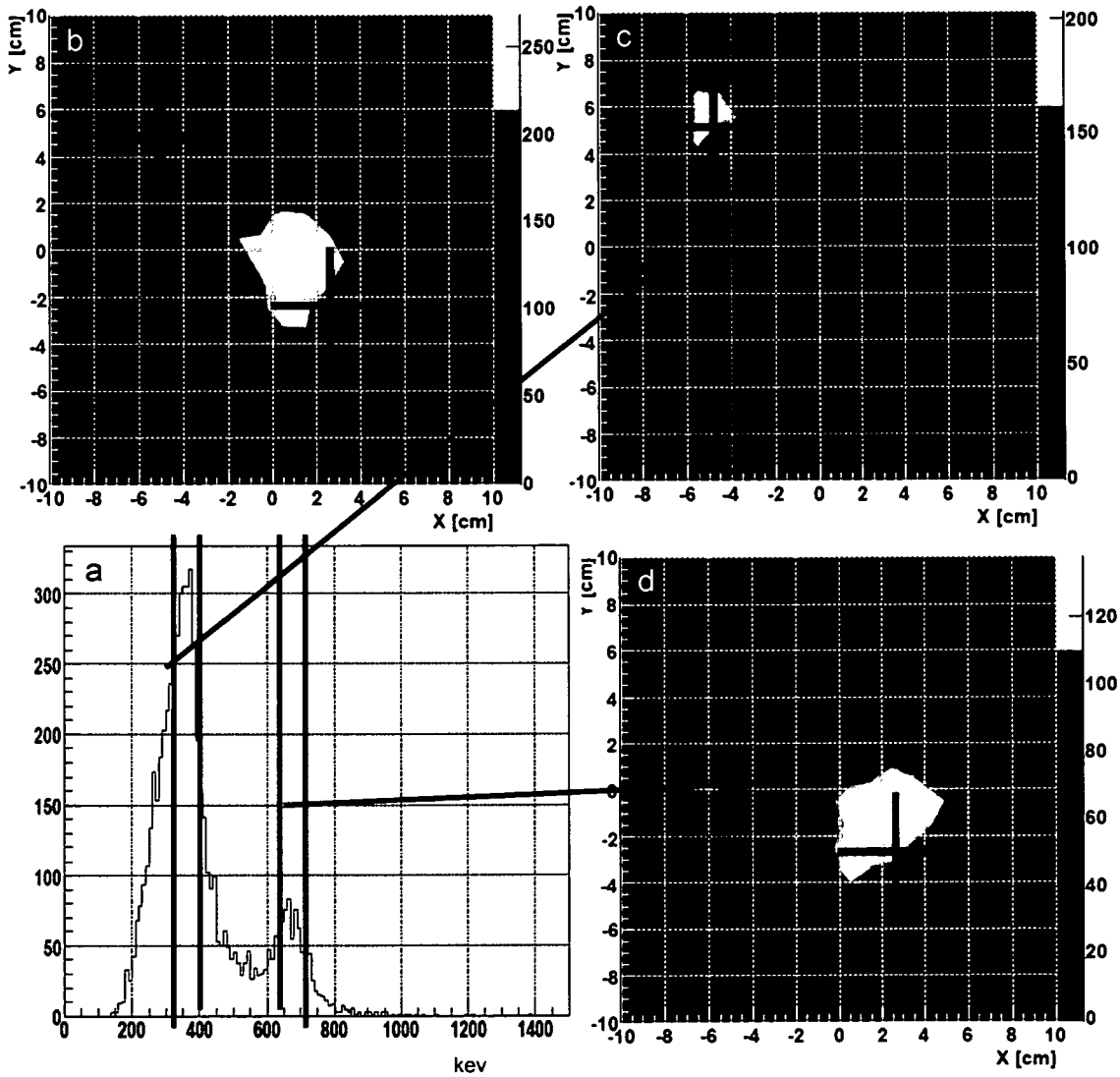

Fig. 4. Images obtained by the simultaneous irradiation of ^{133}Ba: 356 keV and ^{137}Cs: 662 keV.